

Constraints on the primordial gravitational waves with variable sound speed from current CMB data

Cheng Cheng¹ *, Qing-Guo Huang¹ †, Xiao-Dong Li^{1,2} ‡, Yin-Zhe Ma^{3,4} §

¹ State Key Laboratory of Theoretical Physics, Institute of Theoretical Physics, Chinese Academy of Sciences, Beijing 100190, China

² Department of Modern Physics, University of Science and Technology of China, Hefei 230026, China

³ Department of Physics and Astronomy, University of British Columbia, Vancouver, V6T 1Z1, BC Canada

⁴ Canadian Institute for Theoretical Astrophysics, 60 St. George Street Toronto, M5S 3H8, Ontario, Canada

ABSTRACT: We make a comprehensive investigation of the observational effect of the inflation consistency relation. We focus on the general single-field inflation model with the consistency relation $r = -8c_s n_t$, and investigate the observational constraints of sound speed c_s by using the Seven-Year *WMAP* data, the BICEP tensor power spectrum data, and the constraints on $f_{\text{NL}}^{\text{equil.}}$ and $f_{\text{NL}}^{\text{orth.}}$ from the Five-Year *WMAP* observations. We find that the constraints on the tensor-to-scalar ratio r is much tighter if c_s is small, since a large tilt n_t is strongly constrained by the observations. We obtain $r < 0.37$, 0.27 and 0.09 ($dn_s/d\ln k = 0$) for $c_s=1$, 0.1 and 0.01 models at 95.4% confidence level. When taking smaller values of c_s , the positive correlation between r and n_s also leads to slightly tighter constraint on the upper bound of n_s , while the running of scalar spectral index $dn_s/d\ln k$ is generally unaffected. For the sound speed c_s , it is not well constrained if only the CMB power spectrum data is used, while the constraints are obtainable by taking $f_{\text{NL}}^{\text{equil.}}$ and $f_{\text{NL}}^{\text{orth.}}$ priors into account. With the constraining data of $f_{\text{NL}}^{\text{equil.}}$ and $f_{\text{NL}}^{\text{orth.}}$, we find that, $c_s \lesssim 0.01$ region is excluded at 99.7% CL, and the $c_s = 1$ case (the single-field slow-roll inflation) is slightly disfavored at 68.3% CL. In addition, the inclusion of $f_{\text{NL}}^{\text{equil.}}$ and $f_{\text{NL}}^{\text{orth.}}$ into the analysis can improve the constraints on r and n_s . We further discuss the implications of our constraints on the test of inflation models.

KEYWORDS: tensor perturbation, CMB, inflation, consistency relation.

*chcheng@itp.ac.cn

†huangqg@itp.ac.cn

‡renzhe@mail.ustc.edu.cn

§mayinzhe@phas.ubc.ca

Contents

1. Introduction	1
2. Single-field Inflation Model	2
3. Data Analysis Methodology	4
4. Cosmological Constraints of Fixed c_s Models	5
4.1 Effects of c_s on the Power Spectrum	5
4.2 Results of Fitting	6
4.2.1 The $dn_s/d\ln k = 0$ case	6
4.2.2 The $dn_s/d\ln k \neq 0$ case	7
5. Cosmological Constraints of Free c_s Models	8
5.1 Results of fitting Without f_{NL} Prior	8
5.2 Results of fitting With f_{NL} Prior	10
6. Conclusion	12

1. Introduction

An important task of modern cosmology is to understand the expansion history of the Universe. The standard hot big-bang model is successful in explaining various observations, including Hubble expansion, Big-bang Nucleosynthesis and microwave background radiation [1], yet still suffers from the flatness, horizon and monopole problems, etc. The inflation model, in which the vacuum energy drives the Universe exponentially expanding in the very early Universe [2], was proposed under such concerns. Besides the successful explanation of the above problem, inflationary cosmology can provide a viable mechanism for the origin of the cosmic structures.

There have been numerous inflation models proposed in the last several decades. In the face of so many competing candidates, it is necessary to find an effective way to figure out which one is realistic, or at least, which one is most favored by the cosmological observations. Especially, it is important to confirm or rule out the canonical single-field slow-roll (SFSR) inflation model.

It has been proved that the SFSR inflation can generate observable primordial scalar and tensor perturbations, which encode themselves in the cosmic microwave background (CMB) anisotropies. Thus, it is possible to test inflationary models from the current CMB observations, e.g., the Wilkinson Microwave Anisotropy Probe (*WMAP*) satellite [3], QUaD experiment [4], BICEP experiment [5] and other probes [6].

There have been a number of investigations made on testing the inflation models from the current and future CMB observations [7], mainly on the issues of constraining the SFSR model with the scalar spectral index n_s , running of the spectral index $dn_s/d\ln k$, and tensor-to-scalar ratio r as free parameters. Besides the determination of the parameters in inflation models, it has also been proposed [8] that the consistency relations, which features various types of inflation models, can be used as a test to classify and distinguish different models of inflation. The possibility of the observational test of the consistency relations has been discussed in [8] in detail.

In this paper we make further investigations on the observational effect of the consistency relation $r = -8c_s n_t$. We focus on the general single-field inflation model, and discuss the current constraints on the sound speed c_s from the CMB data, including the Seven-Year *WMAP* (WMAP7) power spectrum data [9], the BICEP data [5], and the constraints on $f_{\text{NL}}^{\text{equil.}}$ and $f_{\text{NL}}^{\text{orth.}}$ from the Five-Year *WMAP* (WMAP5) observations [10, 11]. We then discuss the results of the constraints on n_s , r , $dn_s/d\ln k$ parameters when $c_s \neq 1$.

This paper is organized as follows. In Sec. 2, we introduce the inflationary consistency relation in the general single-field inflation model. In Sec. 3, we briefly introduce the CMB data and data analysis methodology used in this paper. The results of constraints on cosmological parameters are presented in Sec. 4 and Sec. 5. We summarize our results in Sec. 6.

2. Single-field Inflation Model

Let's start with the general single-field inflation model

$$S = \int d^4x \sqrt{-g} \left[\frac{M_p^2}{2} R + P(X, \phi) \right], \quad (2.1)$$

where $M_p = 1/\sqrt{8\pi G}$ is the reduced Plack mass, R is the Ricci scalar, g is the determinant of the metric, and $X = -\frac{1}{2}g^{\mu\nu}\partial_\mu\phi\partial_\nu\phi$. $P(X, \phi)$ is an arbitrary function of X and ϕ . This action is the most general Lorentz invariant action for inflaton ϕ minimally coupled to Einstein gravity. The primordial scalar power spectrum of curvature perturbation is [12]

$$\Delta_R^2 = \frac{H^2/M_p^2}{8\pi^2 c_s \epsilon}, \quad (2.2)$$

where

$$\epsilon = -\frac{\dot{H}}{H^2}, \quad (2.3)$$

is the slow-roll parameter, and

$$c_s = \frac{P_{,X}}{P_{,X} + 2XP_{,XX}} \quad (2.4)$$

is the speed of sound. The spectral index of scalar curvature perturbation power spectra becomes

$$n_s - 1 = \frac{d\ln \Delta_R^2}{d\ln k} = -2\epsilon - \eta - s, \quad (2.5)$$

where

$$\eta = \frac{\dot{\epsilon}}{H\epsilon}, \quad s = \frac{\dot{c}_s}{Hc_s}, \quad (2.6)$$

are another two slow-roll parameters. Due to the dynamics of inflation, the spectral index n_s can be scale-dependent as well. Its scale-dependence is measured by the running of the spectral index $dn_s/d\ln k$. The primordial power spectrum of scalar curvature perturbation then takes the form,

$$\Delta_R^2(k) = \Delta_R^2(k_0) \left(\frac{k}{k_0} \right)^{n_s(k_0) - 1 + \frac{1}{2} dn_s/d\ln k}, \quad (2.7)$$

where k_0 is the pivot scale. The primordial power spectrum of gravitational waves perturbation generated during inflation only depends on the Hubble parameter during inflation

$$\Delta_T^2 = \frac{H^2/M_p^2}{\pi^2/2}, \quad (2.8)$$

with tilt

$$n_t = \frac{d \ln \Delta_T^2}{d \ln k} = -2\epsilon. \quad (2.9)$$

The tensor-to-scalar ratio is defined as

$$r = \Delta_T^2/\Delta_R^2 = 16c_s\epsilon, \quad (2.10)$$

and then by combing with Eq. (2.9), we obtain the consistency relation

$$r = -8c_s n_t. \quad (2.11)$$

Here we should note that since the acceleration of scale factor takes the form $\ddot{a} = H^2 a(1-\epsilon)$, inflation only happens if $\epsilon < 1$, therefore from Eqs. (2.9) and (2.11), we know the valid ranges of values for n_t and r as

$$-2 < n_t \leq 0, \quad \text{and} \quad r < 16c_s. \quad (2.12)$$

If $c_s = 1$, the general single-field inflation model reduces to the single-field slow-roll inflation. But if $c_s \ll 1$, the non-trivial sound speed of inflation can generate non-Gaussian modes of perturbation, which results in a large non-local form of bispectrum [13]. Although the non-local form of bispectrum has not been well classified, the two most general types, equilateral type with shape size $f_{\text{NL}}^{\text{equil.}}$, and orthogonal type measured by $f_{\text{NL}}^{\text{orth.}}$, have been widely discussed in literatures [9, 11, 14]. In [14], the observational constraint on the c_s from the bispectrum has been discussed and the requirement from the stability of the field theory ($c_s^2 \geq 0$) implies $f_{\text{NL}}^{\text{orth.}} \leq -0.054 f_{\text{NL}}^{\text{equil.}}$.

3. Data Analysis Methodology

In the following data analysis, we will combine WMAP7 power spectrum [9], with BICEP tensor power spectrum data [5] and bispectrum constraints on $f_{\text{NL}}^{\text{equil.}}$ and $f_{\text{NL}}^{\text{orth.}}$ [10, 11], to constrain inflation consistency relation. The *WMAP* TT power spectrum at $2 \leq l \leq 1200$ is powerful to constrain the cosmological parameters, e.g. n_s and $dn_s/d \ln k$. We also use the *WMAP* TE/EE data at $2 \leq l \leq 800$, and the BB data mainly on large scales $2 \leq l \leq 23$. To be consistent with the *WMAP* results [9], we choose our pivot scale to be $k_0 = 0.002 \text{ Mpc}^{-1}$.

We also use the BICEP tensor power spectrum data which mainly covers the region $21 \leq l \leq 335$. Following the pipelines of [5], we construct the expected bandpowers for the inflation models, and use the lognormal approximation to calculate the χ^2 function,

$$\chi^2(\mathbf{p}) = \left[\hat{\mathbf{Z}}^{BB} - \mathbf{Z}(\mathbf{p})^{BB} \right]^T \left[\mathbf{D}^{BB}(\mathbf{p}) \right]^{-1} \left[\hat{\mathbf{Z}}^{BB} - \mathbf{Z}(\mathbf{p})^{BB} \right], \quad (3.1)$$

where \mathbf{p} is the model parameters, and $\hat{\mathbf{Z}}^{BB}$ and $\mathbf{Z}(\mathbf{p})^{BB}$ are the observational and theoretical bandpowers. $\mathbf{D}^{BB}(\mathbf{p})$ is the covariance matrix which is dependent on the model parameters. The likelihood function then takes the form

$$\mathcal{L} \propto \frac{1}{\sqrt{\det[\mathbf{D}^{BB}(\mathbf{p})]}} e^{-\chi^2(\mathbf{p})/2}. \quad (3.2)$$

In addition, the observational results of $f_{\text{NL}}^{\text{equil.}}$ and $f_{\text{NL}}^{\text{orth.}}$ can also constrain the value of c_s . We use $f_{\text{NL}}^{\text{equil.}}$ and $f_{\text{NL}}^{\text{orth.}}$ priors obtained from the WMAP5 observations [10, 11], and construct the χ^2 function as

$$\chi^2(\mathbf{p}) = v(\mathbf{p})_{\text{WMAP}}^T C^{-1} v(\mathbf{p})_{\text{WMAP}}, \quad (3.3)$$

where C is the covariance matrix given in [11], and $v(\mathbf{p})_{\text{WMAP}}$ is the difference between the observed and model values of $f_{\text{NL}}^{\text{equil.}}$ and $f_{\text{NL}}^{\text{orth.}}$ [11],

$$v(\mathbf{p})_{\text{WMAP}} = \begin{pmatrix} \langle \hat{f}_{\text{NL}}^{\text{equil.}}(\mathbf{p}) \rangle - (\hat{f}_{\text{NL}}^{\text{equil.}})_{\text{WMAP}} \\ \langle \hat{f}_{\text{NL}}^{\text{orth.}}(\mathbf{p}) \rangle - (\hat{f}_{\text{NL}}^{\text{orth.}})_{\text{WMAP}} \end{pmatrix}. \quad (3.4)$$

The WMAP5 data yields to [11]¹

$$f_{\text{NL}}^{\text{equil.}} = 155 \pm 140, \quad f_{\text{NL}}^{\text{orth.}} = -149 \pm 110, \quad (3.5)$$

where the errors given are the 1σ confidence level.

We will determine the best-fit parameters and the 68.3% and 95.4% confidence level (CL) ranges by using the Monte Carlo Markov chain (MCMC) technique. The whole set of our free parameters is

$$\mathbf{P} = \{\Omega_b h^2, \Omega_c h^2, \theta, \tau, n_s, dn_s/d \ln k, r, c_s, A_s, A_{SZ}\}^2. \quad (3.6)$$

¹The covariance matrix C is dependent on the data [11]. Since the WMAP7 covariance matrix C has not yet been published, we will adopt the WMAP5 covariance matrix C in the following discussion.

² θ is the ratio of the sound horizon to the angular diameter distance; τ is the the reionization optical depth; A_s is the primordial superhorizon power in the curvature perturbation on the pivot scale $k_0 = 0.002 \text{ Mpc}^{-1}$; A_{SZ} is an SZ template normalization.

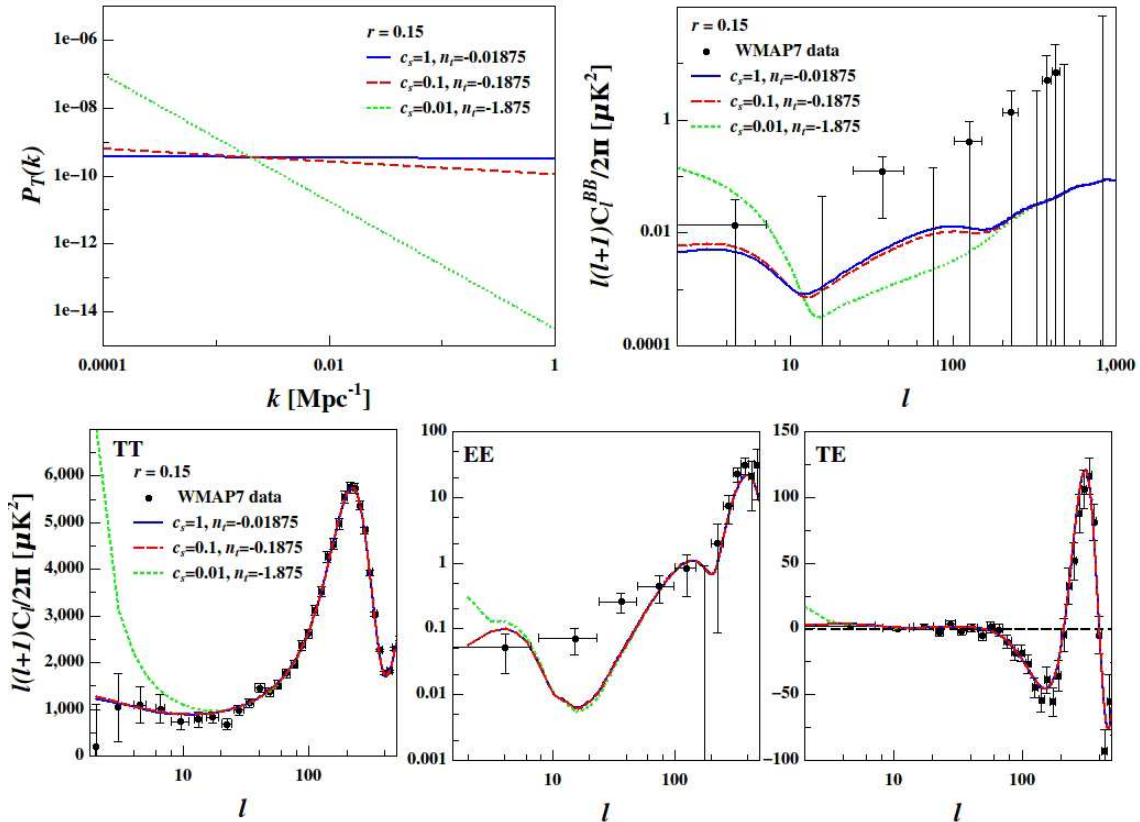


Figure 1: Power spectra for inflation models with different c_s . Models with $c_s=1, 0.1$ and 0.01 are plotted in blue solid, red dashed and green dotted lines, respectively. In all figures we fix $r = 0.15$. The primordial tensor power spectrum and the BB, TT, EE, TE power spectra are plotted. The *WMAP* data [9] are plotted in black points. The $c_s=0.1$ model with $n_t = -0.1875$ leads to slightly larger values of power spectrum at the large scale (not very evident), while the $c_s=0.01$ model leads to significantly larger $P_T(k)/C_l$ s in small- k /low- l region.

We modify the publicly available CAMB [15] and COSMOMC packages [16] to include models with c_s as a free parameter, and generate $O(10^5)$ samples for each set of results presented in this paper.

4. Cosmological Constraints of Fixed c_s Models

In the following sections we will discuss the cosmological interpretations of the consistency relation. In this section we focus on three models with c_s fixed as 1, 0.1 and 0.01. The free c_s model will be discussed in the next section.

4.1 Effects of c_s on the Power Spectrum

We firstly clarify how the different values of c_s affect the shape of the angular power spectra of CMB.

In the upper-left panel of Fig. 1 we plot the primordial tensor power spectrum for $c_s=1, 0.1$ and 0.01 respectively. We see that c_s has significant influence on the tilt of the

power spectrum through the consistency relation $n_t = -r/(8c_s)$. In particular, at the large scale (small k), the $c_s=0.01$ and $c_s=0.1$ models have much larger values of $P_t(k)$ than that in the model with $c_s = 1$.

This effect is also visible in BB , TT , EE and TE power spectra, which is shown in the upper-right and lower panels of Fig. 1 (with lensing). In all figures we take $r = 0.15$ and fix other parameters at their WMAP7 best-fit values. It is shown that the amplitude of the power spectrum for $c_s=0.1$ is slightly larger than the $c_s=1$ case (not evident), while for the $c_s=0.01$ case the low- l C_l s are significantly larger. The panels indicate that the set of parameters $r = 0.15$, $c_s = 0.01$ is inconsistent with the *WMAP* data. Thus, we expect a tight constraint on r when c_s is small.

4.2 Results of Fitting

Our results of fitting for different models with fixed c_s are shown in Table 1.

Table 1: Results of fitting with fixed c_s .

Data & Model		$r(95.4\% \text{ CL})$	$n_t(95.4\% \text{ CL})$	n_s	$dn_s/d \ln k$
<i>WMAP</i>	$c_s = 1$	< 0.37	> -0.05	$0.967^{+0.026}_{-0.010}$	–
	$c_s = 0.1$	< 0.26	> -0.33	$0.972^{+0.016}_{-0.014}$	–
	$c_s = 0.01$	< 0.09	> -1.16	$0.966^{+0.017}_{-0.010}$	–
<i>WMAP+BICEP</i>	$c_s = 1$	< 0.32	> -0.04	$0.966^{+0.024}_{-0.008}$	–
	$c_s = 0.1$	< 0.26	> -0.33	$0.971^{+0.019}_{-0.014}$	–
	$c_s = 0.01$	< 0.09	> -1.16	$0.969^{+0.014}_{-0.013}$	–
<i>WMAP+BICEP</i> ($+dn_s/d \ln k$)	$c_s = 1$	< 0.36	> -0.05	$1.011^{+0.050}_{-0.035}$	$-0.023^{+0.018}_{-0.024}$
	$c_s = 0.1$	< 0.35	> -0.44	$1.014^{+0.070}_{-0.046}$	$-0.022^{+0.021}_{-0.034}$
	$c_s = 0.01$	< 0.10	> -1.21	$1.005^{+0.068}_{-0.013}$	$-0.019^{+0.005}_{-0.030}$

Here we list the results for $c_s=1$, 0.1 and 0.01. In the 4-9 rows, the constraints on r , n_t , n_s and $dn_s/d \ln k$ by using the *WMAP+BICEP* data are listed, divided into the $dn_s/d \ln k = 0$ and $dn_s/d \ln k \neq 0$ cases. For comparison, in the 1-3 rows we also list the results obtained by using the *WMAP* data alone with $dn_s/d \ln k = 0$. We discuss the results of constraints in Sec. 4.2.1 and 4.2.2 in detail.

4.2.1 The $dn_s/d \ln k = 0$ case

In this subsection we briefly discuss the fitting results of models without including $dn_s/d \ln k$ as a free parameter.

Let us first see the constraints on the tensor-to-scalar ratio r which determines the amplitude of the tensor power spectrum. The fitting results of r are listed in the second column of Table 1 and the likelihood functions are plotted in the left panel of Fig. 2. Using the *WMAP* data alone, we find a 95.4% CL constraint $r < 0.37$, which is well consistent with the result obtained by the *WMAP* 7-yr data ($r < 0.36$). As expected, we find the constraint on r becomes much tighter if the value of c_s becomes smaller (see the left panel of Fig. 2). Using the *WMAP+BICEP* data, we find $r < 0.32$, 0.26 and 0.09 (95.4% CL) for $c_s = 1$, 0.1 and 0.01, respectively. This result is quite reasonable. According to the consistency relation $n_t = -r/(8c_s)$, if c_s is small, a large r would lead to a large n_t , leading

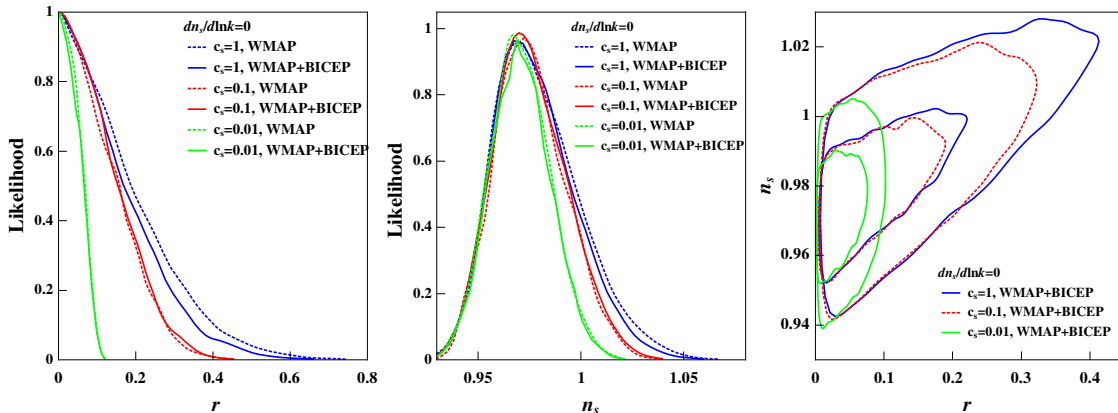


Figure 2: Fitting results for the fixed c_s models with $dn_s/d\ln k = 0$. In the left and middle panels we plot the likelihoods of r and n_s for the $c_s = 1, 0.1, 0.01$ models in blue, red, green lines, and the results obtained by using the *WMAP* and *WMAP+BICEP* are shown in dotted and solid lines, respectively. In the right panel we also plot the marginalized 68.3% and 95.4% CL contours in the $r - n_s$ plane. We see that smaller values of c_s lead to tighter constraints on r , and thus tighter upper bound constraints on n_s , due to their correlation. The inclusion of BICEP data slightly improves the constraints on r and n_s for the $c_s = 1$ case.

to a large tensor mode on superhorizon scale, which is strongly constrained by low- l CMB data. The necessary condition for inflation Eq. (2.12) is automatically satisfied by the constraint. The $r = 0.15$, $c_s = 0.01$ case shown in the Fig. 1 is excluded.

Except for r , another interesting issue is the fitting results of the scalar spectral index n_s . Using the *WMAP+BICEP* data, we find $n_s = 0.966^{+0.024}_{-0.008}$, $0.971^{+0.019}_{-0.014}$ and $0.969^{+0.014}_{-0.013}$ (68.3% CL) for $c_s = 1, 0.1$ and 0.01 . All the results are consistent with Harrison-Zeldovich spectrum ($n_s = 1$) at 68.3% CL. The likelihoods of n_s in different cases are plotted in the middle panel of Fig. 2. Similar to r , we find that the upper bound constraint on n_s also becomes tighter when c_s is smaller. This effect is caused by the positive correlation between r and n_s . In the right panel of Fig. 2, we plot the marginalized contours in the $r - n_s$ plane, which shows that the smaller c_s is, the tighter constraints on n_s and r .

The results of constraints from BICEP data are as follows. For the $c_s=1$ model, we get $r < 0.37(0.32)$ (95.4% CL) by using the *WMAP*(*WMAP+BICEP*) data. The inclusion of BICEP data slightly improves the constraint by $\sim 14\%$. However, for the $c_s = 0.1$ and 0.01 cases, since the constraints on r mainly come from constraints on n_t by the low- l *WMAP* data, the inclusion of BICEP data does not lead to significant improvement in the result³. The BICEP data can only affect n_s through its correlation between r , so it does not have significant effect on the results of n_s .

4.2.2 The $dn_s/d\ln k \neq 0$ case

We now discuss the results of constraints with running of spectral index $dn_s/d\ln k$ as a free parameter.

³The Two-Year BICEP data, which maps only $\sim 2\%$ of the sky, measures limited modes of perturbations, therefore does not contribute too much on the total constraining.

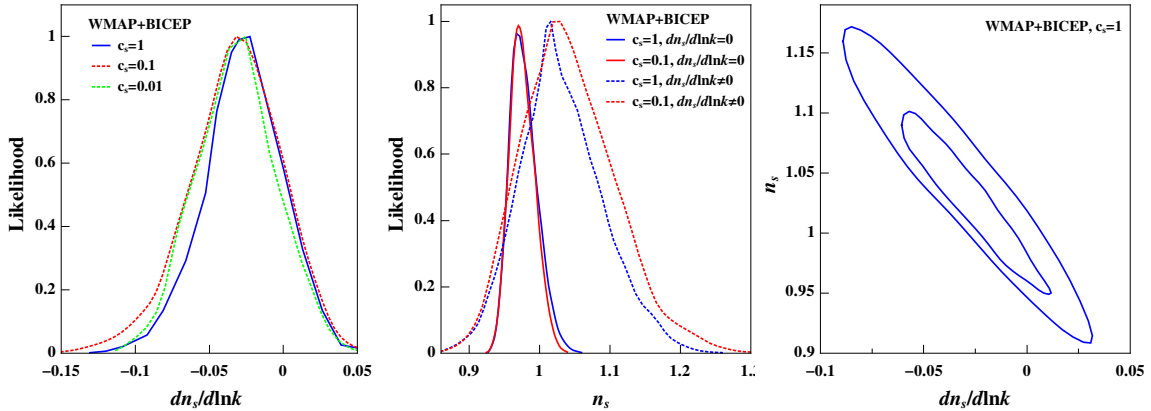


Figure 3: Fitting results for the fixed c_s models with $dn_s/d \ln k \neq 0$. The marginalized likelihoods of $dn_s/d \ln k$ and n_s are shown in the left and middle panels. In the right panel we plot the marginalized 68.3% and 95.4% CL contours in the $dn_s/d \ln k - n_s$ plane. The influence of c_s on $dn_s/d \ln k$ is not very significant (left panel). The inclusion of $dn_s/d \ln k$ significantly amplifies the allowed range of n_s and shifts its central value from below 1 to above 1 (middle panel), since they are strongly anti-correlated (right panel; see also Eq. (2.7)).

The fitting results are shown in the last three rows of Table 1 and Fig. 3. For the three models we find similar constraints on $dn_s/d \ln k$, thus c_s does not have too much influence on $dn_s/d \ln k$.

The most striking effect of the inclusion of $dn_s/d \ln k$ is the significant amplification of the allowed region of n_s . In the middle panel of Fig. 3, we plot the likelihood functions of n_s for $dn_s/d \ln k = 0$ (solid) and $dn_s/d \ln k \neq 0$ (dotted). We see that the width of n_s likelihood is increased by nearly a factor of two. The inclusion of $dn_s/d \ln k$ also changes the central values of n_s from below 1 to above 1. These phenomena are caused by the strong anti-correlation between $dn_s/d \ln k$ and n_s (see the right panel of Fig. 3).

The inclusion of $dn_s/d \ln k$ slightly releases the upper bound constraints of r . For the $c_s = 1, 0.1, 0.01$ models, the 95.4% CL upper bounds on r are 0.32, 0.26, 0.09 for $dn_s/d \ln k = 0$ and 0.36, 0.35, 0.10 for $dn_s/d \ln k \neq 0$.

5. Cosmological Constraints of Free c_s Models

In this section we consider the more general case, i.e., treating c_s as a free parameter.⁴ We not only use the *WMAP* and *BICEP* power spectrum data, but also take $f_{\text{NL}}^{\text{equil.}}$ and $f_{\text{NL}}^{\text{orth.}}$ into consideration in order to constrain c_s . A summary of the fitting results, including c_s , r , n_t , n_s and $dn_s/d \ln k$ are given in Table 2. Notice that the word ‘UCON’ represents for ‘unconstrained’.

5.1 Results of fitting Without f_{NL} Prior

In this subsection we discuss the results obtained by *WMAP*+*BICEP* data, without adding

⁴We sample c_s in the range of (0.001,1).

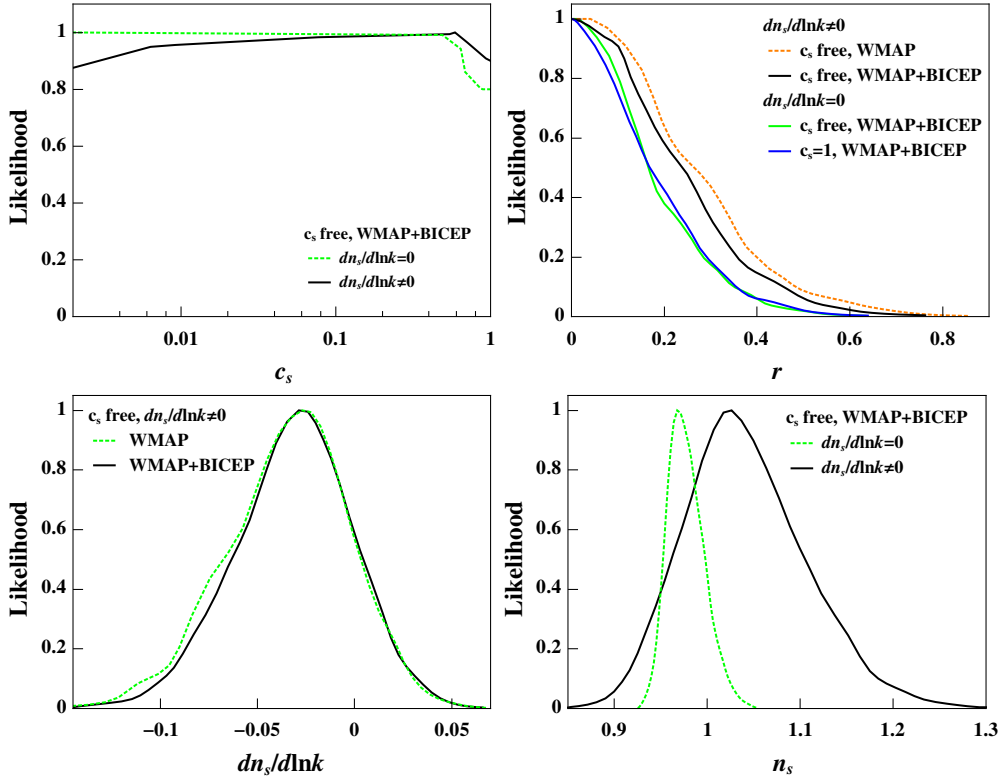


Figure 4: Marginalized likelihoods of c_s , r , $dn_s/d \ln k$ and n_s for the free c_s case, obtained by using the *WMAP* and *WMAP+BICEP* data. Upper-left: The current CMB power spectrum data alone can not constrain c_s . Upper-right: The inclusion of $dn_s/d \ln k$ slightly widen the distribution of r . Lower-left: The inclusion of BICEP data does not affect the distribution of $dn_s/d \ln k$ too much. Lower-right: The inclusion of $dn_s/d \ln k$ greatly boardens the width of n_s likelihood, and shifts its central value to be greater than unity.

Table 2: Results of fitting with c_s as a free parameter.

Data & Model		c_s	r (95.4% CL)	n_t (95.4% CL)	n_s	$dn_s/d \ln k$
<i>WMAP</i>		UCON	< 0.36	> -1.33	$0.966^{+0.024}_{-0.011}$	–
	+ $dn_s/d \ln k$	UCON	< 0.46	> -1.44	$1.027^{+0.065}_{-0.051}$	$-0.026^{+0.023}_{-0.030}$
<i>WMAP+BICEP</i>		UCON	< 0.32	> -1.30	$0.967^{+0.025}_{-0.012}$	–
	+ $dn_s/d \ln k$	UCON	< 0.41	> -1.40	$1.019^{+0.063}_{-0.038}$	$-0.026^{+0.020}_{-0.027}$
<i>WMAP+BICEP</i> + f_{NL}		$0.019^{+0.012}_{-0.006}$	< 0.21	> -0.91	$0.973^{+0.011}_{-0.016}$	–
	+ $dn_s/d \ln k$	$0.016^{+0.017}_{-0.003}$	< 0.29	> -1.15	$1.016^{+0.064}_{-0.045}$	$-0.024^{+0.022}_{-0.033}$

$f_{NL}^{\text{equil.}}$ and $f_{NL}^{\text{orth.}}$ priors into the analysis. The fitting results of parameters are shown in the 1-4 rows of Table 2, and the likelihoods of c_s , r , n_s and $dn_s/d \ln k$ are plotted in Fig. 4.

Let us first have a look at the constraint on c_s , and its likelihood is plotted in the upper-left panel of Fig. 4. The current CMB power spectrum data is not able to constrain on c_s , and the likelihood function shows that it can take any possible value given the current constraints.

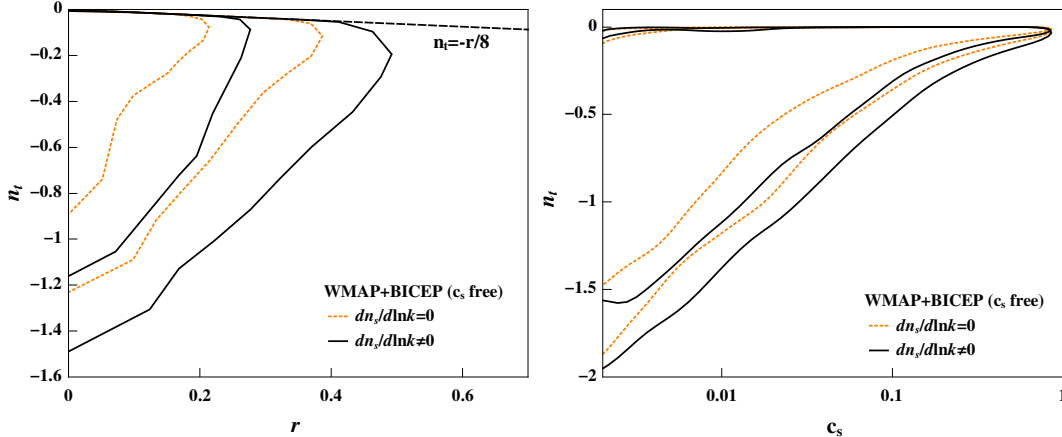


Figure 5: Marginalized 68.3% and 95.4% CL contours in the $r - n_t$ (left) and $c_s - n_t$ (right) planes which are obtained by using the *WMAP*+*BICEP* data. In the left panel, the $n_t = -\frac{r}{8}$ line is plotted in the black dashed line. We see that $n_t > -2$ automatically satisfied, and the inclusion of $dn_s/d \ln k$ evidently amplifies the parameter space.

Secondly, the likelihoods of r are shown in the upper-right panel of Fig. 4. We see the green and blue lines are close to each other, which means that the constraint on r with free c_s is similar to the result for $c_s=1$.⁵ We get $r < 0.32$ (95.4% CL) for both $c_s = 1$ and c_s free models (*WMAP*+*BICEP*, $dn_s/d \ln k = 0$). The inclusion of *BICEP* data slightly improves constraint of r from 0.36 to 0.32 ($dn_s/d \ln k = 0$). We see the inclusion of $dn_s/d \ln k$ as a free parameter boardens the width of distribution of r . At 95.4% CL, the constraint is widened from $r < 0.32$ to $r < 0.41$ (*WMAP*+*BICEP*).

Thirdly, in the lower panels of Fig. 4 we plot the marginalized likelihoods of $dn_s/d \ln k$ (left) and n_s (right). We find that the results are similar to the fixed c_s models. It implies that the *BICEP* data almost does not affect the constraint of $dn_s/d \ln k$, and the inclusion of $dn_s/d \ln k$ greatly amplifies the distribution of n_s and shifts its central value to above 1.

In addition, in Fig. 5 we plot the marginalized 2D-contours in the $r - n_t$ (left) and $c_s - n_t$ (right) planes. The slow-roll model with $n_t = -r/8$ is plotted in the black dashed line in the left panel, and the $dn_s/d \ln k = 0$ and $dn_s/d \ln k \neq 0$ cases are shown in orange dotted and black solid lines, respectively. By releasing c_s as a free parameter, n_t ranges to much smaller values (~ -1 to -1.5 at 95.4% CL), especially in the small c_s region. We find $n_t > -2$ is still satisfied by the constraints. In both panels we see the inclusion of $dn_s/d \ln k$ boardens the ranges of the parameter space.

5.2 Results of fitting With f_{NL} Prior

In this subsection let us take the $f_{\text{NL}}^{\text{equil.}}$ and $f_{\text{NL}}^{\text{orth.}}$ priors into account. The fitting results are shown in the last two rows of Table 2, and the likelihoods of c_s , r , n_s and $dn_s/d \ln k$ are plotted in Fig. 6.

⁵A similar conclusion was obtained in [17].

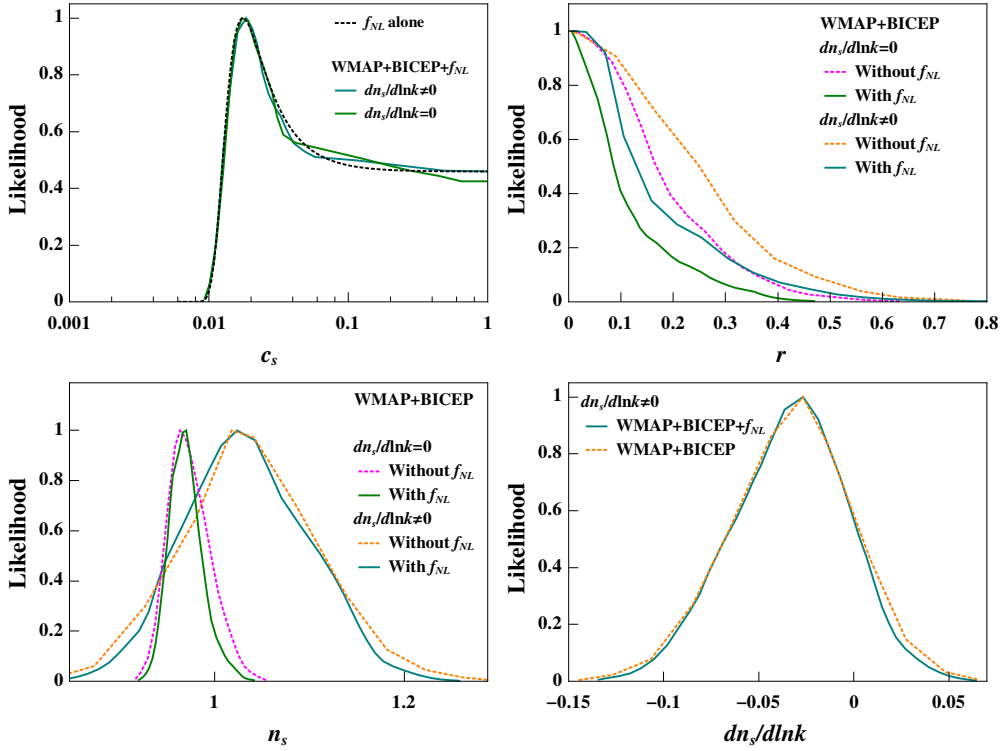


Figure 6: Marginalized likelihoods of c_s , r , n_s and $dn_s/d\ln k$ for the c_s free case from *WMAP*+*BICEP* data. The inclusion of f_{NL} prior evidently tightens the constraints on c_s and r , and slightly improves the upper-bound constraint on n_s . The running of the spectral index $dn_s/d\ln k$ remains unchanged.

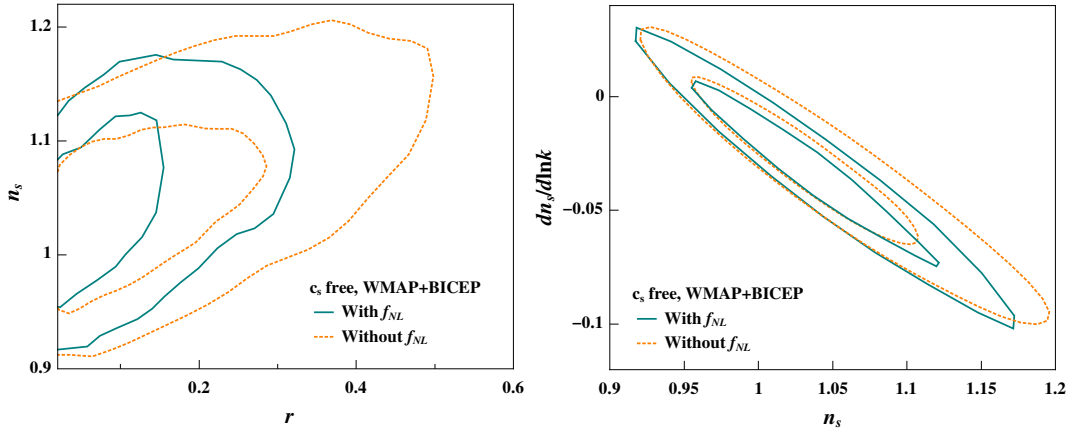


Figure 7: Marginalized 68.3% and 95.4% CL contours in the $r - n_s$ (left) and $n_s - dn_s/d\ln k$ (right) planes, obtained by using the *WMAP*+*BICEP* data. In all figures we let $dn_s/d\ln k$ and c_s as free parameters. The constraints with and without f_{NL} cases are shown in dark cyan solid and orange dotted colors respectively.

The most striking effect is that the inclusion of $f_{NL}^{\text{equil.}}$ and $f_{NL}^{\text{orth.}}$ significantly improves the constraint on c_s . At 68.3% CL, we obtain $0.013 < c_s < 0.031$ and $0.013 < c_s < 0.033$

for the cases of without and with $dn_s/d\ln k$ as a free parameter. We find the large c_s region, including the SFSR inflation with $c_s = 1$, is slightly disfavored at around 68.3% CL, while $c_s \lesssim 0.01$ is excluded at 99.7% CL. Thus, the bispectrum data is much more powerful than the power spectrum data for constraining c_s .

By narrowing the allowed range of c_s , the addition of $f_{\text{NL}}^{\text{equil.}}$ and $f_{\text{NL}}^{\text{orth.}}$ also has interesting effect on constraining the other parameters. The likelihood of r is shown in the upper-right panel of Fig. 6. We see that, once $f_{\text{NL}}^{\text{equil.}}$ and $f_{\text{NL}}^{\text{orth.}}$ priors are considered, the constraint becomes much tighter. This can be also seen through the contours in the left panel of Fig. 7. Again, due to the correlation between r and n_s , where $f_{\text{NL}}^{\text{equil.}}$ and $f_{\text{NL}}^{\text{orth.}}$ priors are included a slightly tighter constraint on the upper bound of n_s is also obtained (see the lower-left panel of Fig. 6). But the effect of $f_{\text{NL}}^{\text{equil.}}$ and $f_{\text{NL}}^{\text{orth.}}$ priors on $dn_s/d\ln k$ is negligible (see the lower-right panels of Fig. 6).

Finally, the correlations between r , n_s and $dn_s/d\ln k$ are shown in Fig. 7. The left panel shows the $r - n_s$ contours and the right panel shows the $n_s - dn_s/d\ln k$ contours. In all figures we set c_s , $dn_s/d\ln k$ as free parameters and use both *WMAP* and BICEP data. The cases of without and with f_{NL} as a free parameter are shown in orange and dark cyan colors. One can see the strong correlation between r and n_s , which suggests that if the distribution of r is tightened, n_s distribution is also constrained. However, the distribution of running spectral index $dn_s/d\ln k$, is not much affected by this correlation, because the change of n_s is much smaller comparing with r .

6. Conclusion

In this paper we make a detailed investigation of the cosmological interpretation of the consistency relation from CMB data. We focus on the general single-field inflation model in which the spectral index n_t of tensor perturbation power spectrum is related to the tensor-to-scalar ratio r by $n_t = -r/(8c_s)$, and further investigate the effect of the sound speed c_s . The datasets used in this paper include the *WMAP* power spectrum data, the BICEP *B*-mode polarization data, and $f_{\text{NL}}^{\text{equil.}}$ and $f_{\text{NL}}^{\text{orth.}}$ priors obtained from the WMAP5 bispectrum data.

We discuss three models with fixed $c_s=1, 0.1$ and 0.01 . We find that when c_s is small, the tilt of the tensor power spectrum n_t becomes very large if r is not too small, and then a tight constraint on r is obtained for $c_s \ll 1$. Using the *WMAP*+BICEP data, we obtain the 95.4% CL constraints of $r < 0.37, 0.26, 0.09$ for the $c_s=1, 0.1, 0.01$ cases ($dn_s/d\ln k = 0$). Due to the positive correlation between r and n_s , smaller values of c_s lead to slightly tighter constraint on the upper bound of n_s . The effect of c_s on the running of scalar spectral index $dn_s/d\ln k$ is not obvious. The inclusion of $dn_s/d\ln k$ significantly alters the constraints of n_s , and slightly amplifies the upper bound constraint of r .

For more general cases in which c_s is taken as a free parameter, we find that c_s unconstrained if we only use the current CMB power spectrum data in the analysis, and the marginalized distribution of r , n_s and $dn_s/d\ln k$ are all similar to the $c_s = 1$ case. However, after taking $f_{\text{NL}}^{\text{equil.}}$ and $f_{\text{NL}}^{\text{orth.}}$ priors into consideration, we find the sound speed c_s is effectively constrained. The $c_s \lesssim 0.01$ region is ruled out, and the $c_s \gtrsim 0.03$ region

is disfavored at the 68.3% CL. From the constraints on c_s , the inclusion of f_{NL} leads to tighter constraint on the r and n_s . In the $dn_s/d\ln k = 0$ case, we find $r < 0.21/0.32$ (95.4% CL) with/without f_{NL} prior ($dn_s/d\ln k = 0$), and the results for the $dn_s/d\ln k \neq 0$ case is $r < 0.29/0.41$. The running of spectral index $dn_s/d\ln k$ is almost unaffected.

To summarize, we find that the consistency relation has significant effect in the constraints on cosmological parameters r and n_s when c_s is small, while the parameter $dn_s/d\ln k$ remains unaffected. Although the sound speed c_s is unconstrained by the CMB power spectrum data, it can be effectively constrained by the CMB bispectrum data. Using the $f_{\text{NL}}^{\text{equil.}}$ and $f_{\text{NL}}^{\text{orth.}}$ priors obtained from the WMAP5 data, we find the SFSR model with $c_s=1$ is slightly disfavored at the 68.3% CL. Thus, we are expecting that, the on-going and upcoming CMB observations, such as *Planck* [18] and *CMBPol* [19], with much lower instrumental noise and better foreground clean, will provide stronger constraints on inflation models.

Acknowledgments

QGH is supported by the project of Knowledge Innovation Program of Chinese Academy of Science and a grant from NSFC (grant NO. 10975167). The MCMC is mainly performed by the Lenovo Shenteng 7000 supercomputer in the Supercomputing Center of Chinese Academy of Sciences (SCCAS). XDL acknowledge the Institute of Theoretical Physics and the Supercomputing Center of USTC for the use of computing resources.

References

- [1] S. Weinberg, (Oxford University Press, New York, 2008).
- [2] A. H. Guth, Phys. Rev. D **23**, 347 (1981); A. D. Linde, Phys. Lett. B **108**, 389 (1982); D. H. Lyth and A. Riotto, Phys. Rep. **314**, 1 (1999).
- [3] C. L. Bennett *et al.*, Astrophys. J. Suppl. **148**, 1 (2003); G. Hinshaw *et al.*, Astrophys. J. Suppl. **170**, 288 (2007); E. Komatsu *et al.*, Astrophys. J. Suppl. **192**, 18 (2011).
- [4] M. L. Brown *et al.*, Astrophys. J. **705**, 978 (2009).
- [5] H. C. Chiang *et al.*, Astrophys. J. **711**, 1123 (2010).
- [6] J. Kovac *et al.*, Nature (London) **420**, 772 (2002); A. C. S. Readhead *et al.*, Science **306**, 836 (2004); C. Bischoff *et al.* (CAPMAP Collaboration), Astrophys. J. **684**, 771 (2008); W. C. Jones *et al.*, Astrophys. J. **647**, 823 (2006); J. H. P. Wu *et al.*, Astrophys. J. **665**, 55 (2007).
- [7] L. Knox, Phys. Rev. D **60**, 103516 (1999). H. V. Peiris *et al.*, Astrophys. J. Suppl. Ser. **148**, 213 (2003); S. Chongchitnan and G. Efstathiou, Phys. Rev. D **73**, 083511 (2006); L. Verde, H. Peris and R. Jimenez, JCAP **0601**, 019 (2006); D. Baumann *et al.*, AIP Conf. Proc. **1141**, 10 (2009); Y. Z. Ma, W. Zhao and M. L. Brown, JCAP **1010**, 007 (2010); M. J. Mortonson, H. V. Peiris and R. Easther, Phys. Rev. D **83**, 043505 (2011).

- [8] W. Zhao and Q. -G. Huang, *Class. Quantum Gravet.* **28**, 235003 (2011).
- [9] E. Komatsu *et al.*, *Astrophys. J. Suppl.* **192**, 18 (2011).
- [10] E. Komatsu *et al.*, *Astrophys. J. Suppl.* **180**, 330 (2009); K. M. Smith, L. Senatore and M. Zaldarriaga, *JCAP* **0909**, 006 (2009).
- [11] L. Senatore, K. M. Smith and M. Zaldarriaga, *JCAP* **01**, 028 (2010).
- [12] J. Garriga and V. F. Mukhanov, *Phys. Lett. B* **458**, 219 (1999).
- [13] X. Chen, M. -x. Huang, S. Kachru and G. Shiu, *JCAP* **0701**, 002 (2007).
- [14] Q. -G. Huang, *JCAP* **1005**, 016 (2010).
- [15] A. Lewis, *Phys. Rev. D* **70**, 043011 (2004); A. Lewis, A. Challinor and A. Lasenby, *AJ* **538**, 473 (2000); <http://www.camb.info>
- [16] A. Lewis and S. Bridle, *Phys. Rev. D* **66**, 103511 (2002); <http://cosmologist.info/cosmome/>
- [17] Z. -K. Guo and D. J. Schwarz, *Phys. Rev. D* **81**, 123520 (2010).
- [18] Planck Collaboration, *The Scientific Programme of Planck* [astro-ph/0604069].
- [19] D. Baumann *et al.*, *AIP Conf. Proc.* **1141**, 10 (2009).